CrossMark

ORIGINAL RESEARCH PAPER

Approximate recovery of residual displacement from the strong motion recordings of the 24 August 2016 Amatrice, Italy earthquake

Reeves Whitney[1]

Abstract This paper presents an investigation into the residual ground displacements recorded on a strong motion network during the Mw 6.0 24 August 2016 Amatrice, Italy earthquake. The available accelerometric data from near field recording stations are processed using two different techniques to remove baseline offsets and retain the low frequency signal which depends on residual displacement. The first method uses acausal filtering to identify and retain a dominant pulse while the second method uses linear regression to remove velocity or displacement baseline trends. The results are compared to high-rate (1 and 10 Hz) global positing system (GPS) displacement waveforms, consensus GPS displacement offsets and crustal deformations detected by interferometric synthetic aperture radar (InSAR) satellite imaging. Since the GPS sensors are not all collocated with the accelerometers, the InSAR data is used for stations where no GPS results are available, or when the nearest GPS is far. It is shown that both methods investigated in this paper provide displacement waveforms with features matching those of the high-rate GPS. In addition, the residual displacement magnitudes are in good agreement with the consensus and InSAR displacements. The acceleration time series for the stations considered in this work are provided as an electronic supplement with this paper.

✉ Reeves Whitney
  reeves.whitney@manhattan.edu

[1] Department of Civil and Environmental Engineering, Manhattan College, 4513 Manhattan College Parkway, Riverdale, NY 10471, USA

1 Introduction

At 1:36:32 UTC a Mw 6.0 earthquake occurred in Central Italy causing fatalities of nearly 300 and significant damage to infrastructure, particularly in Amatrice and Arquata del Tronto (Pischiutta et al. 2016; INGV 2017). In Amatrice, the large stock of unreinforced masonry buildings were particularly vulnerable due to poor quality masonry and lack of appropriate connections and anchorage (Fiorentino et al. 2017). The epicenter of the earthquake (42.7° N, 13.23° E) is approximately 1 km West of Accumoli (INGV 2017). This event occurred on a Quarternary normal fault, with NNW-SSE orientation through the Apennines, at a shallow depth of 8 km (Michele et al. 2016; Luzi et al. 2017; Chiaraluce et al. 2017). Fault geometry has been by determined by Tinti et al. (2016) as 26 km long by 16 km wide with 156° strike and 50° dip. High geodetic deformation rates on the order of 4 mm/year have been observed in the region (Cheloni et al. 2016). There is a history of moderate-to-large earthquakes about Mw 5.0–Mw 7.0 in the Central Apennines. This event occurs in a gap between the 26 September 1997 Colfiorito Mw 6.0 sequence to the north and the 6 April 2009 L'Aquila Mw 6.3 sequence to the south (Michele et al. 2016). Figure 1 contains the location of the epicenter and the surface projection of the fault plane. Aftershocks were produced at a rate of about 500 per day until the middle of September when the rate dropped to about 100 per day (Michele et al. 2016). The largest aftershock of Mw 5.9 occurred on 26 October 2016, which preceded the largest event (Mw 6.5) of the
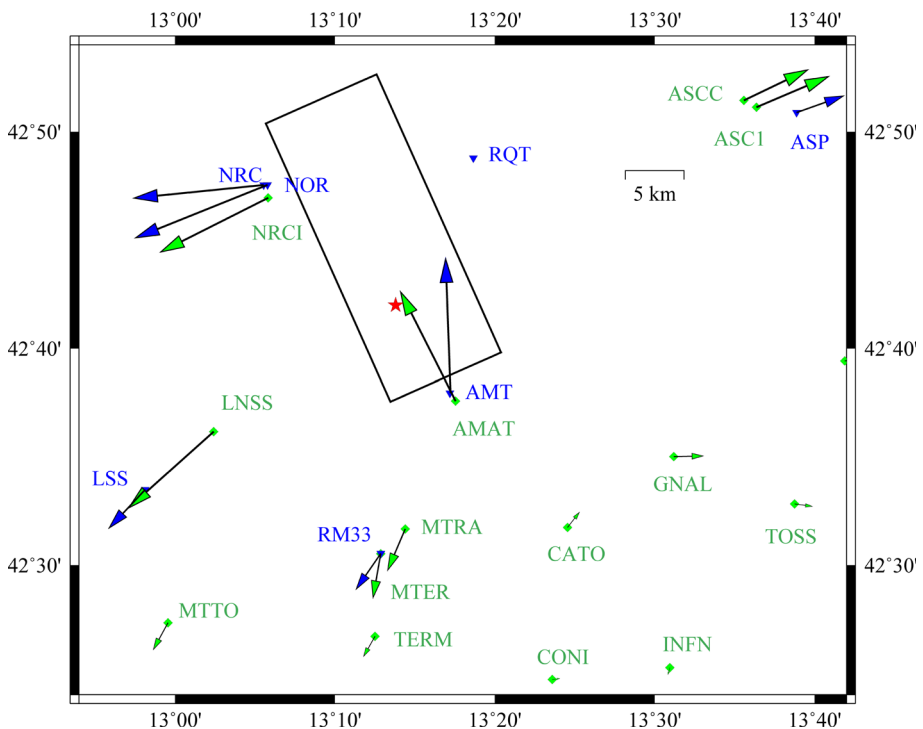
Fig. 1 Map showing the location of the epicenter (red star), SMA stations (blue triangles), GPS stations (green diamonds), and fault plane projection (black polygon). The blue and green vectors represent the resultant horizontal coseismic displacement from SMA and GPS data, respectively

sequence on 30 October 2016. This paper focuses on recovering residual ground displacement from the accelerometric data from the 24 August 2016 event.

The Italian Accelerometric Network (RAN) has made available about 259 strong-motion acceleration (SMA) recordings of this event (ReLUIS-INGV 2016). There are 14 records within an epicentral distance of 30 km and 42 records within 50 km (Lanzano et al. 2016). Near-field records generally match well to the peak ground acceleration (PGA) ground motion prediction equations (GMPEs), while the far-field records (> 80 km) exceed the PGA GMPEs (Lanzano et al. 2016). Peak ground velocity (PGV) and long period spectral acceleration (SA) of the recordings also tend to exceed the GMPEs (Lanzano et al. 2016). Luzi et al. (2017) and Lanzano et al. (2016) have presented an extensive review of the ground motion characteristics, including comparison to GMPEs, spectral response characteristics, comparison to the Italian seismic code, and single side velocity pulse extraction. Peak ground acceleration (PGA) ≈ 400 cm/sec^2 were recorded at Arquata del Tronto (RQT station) and Norcia (NRC station) while the largest PGA ≈ 850 cm/sec^2 was recorded at Amatrice (AMT station). Although, it should be noted that the RQT station is designated as "bad quality record" on the Engineering Strong Motion Database (ESM http://esm.mi.ingv.it/) (Luzi et al. 2016). Upon review of the RQT station, the Up and East components appear reliable but the North signal is clearly unreliable with a PGA ≈ 0.1 cm/sec^2 and signal to noise ratio (SNR) from zero to ~ -5 dB at frequencies below about 5 Hz. Nevertheless, RQT station is of interest because of it epicentral distance (R_{epi}) of 14 km. Table 1 contains epicentral distances, peak ground acceleration (PGA), velocity (PGV), and displacement (PGD) based on the processed records available at ESM, and this work. The primary difference is that the processing procedures on the ESM data removes any residual displacement from the time series.

In addition to the SMA network, ground displacements have been recorded by high-rate global positioning system (HRGPS) and interferometric synthetic aperture radar (InSAR) satellite imaging. GPS data is available in two forms: consensus and time-series. The consensus offset represents the coseismic deformation calculated from GPS position data by averaging 15 days prior and 3 days after the mainshock (Cheloni et al. 2016). The GPS data was analyzed using three different software packages: BERNESE, GAMIT, and GIPSY. A "consensus" between the three solutions is determined after "a comparison and validation process with repeated feedback between the three different analysis centers" (Cheloni et al. 2016). Consensus data gives a displacement offset along with the uncertainty for three translational directions at 106 locations (INGV 2016). There are five GPS stations with displacement in any direction larger than 1 cm: AMAT (Amatrice), ASC0

Table 1 Epicentral distances and peak quantities

Station	R_{epi} (km)	ESM database			This study		
		PGA (g)	PGV (cm/s)	PGD (cm)	PGA (g)	PGV (cm/s)	PGD (cm)
AMT	8.5	0.867	43.5	8.54	0.879	43.5	12.06
ASP	37.8	0.088	3.5	0.96	0.089	3.6	2.28
LSS	26.7	0.023	2.3	0.99	0.024	2.3	1.76
NOR	15.6	0.249	27.1	6.90	0.251	26.9	8.76
NRC	15.3	0.374	29.8	6.62	0.374	29.4	7.71
RM33	21.1	0.102	9.3	2.40	0.102	9.3	2.73

(Ascoli Piceno), ASCC (Ascoli Piceno), LNSS (Leonessa) and NRCI (Norcia). These consensus results will be used for comparison to the nearest SMA stations. In addition, the station MTER will be considered since the displacement is just under 1 cm, but it is collocated with SMA station RM33. Figure 1 shows the locations of the SMA stations and recovered approximate displacements (blue triangles, vectors) along with the GPS stations and offsets (green diamonds, vectors).

Although the consensus offsets are useful for comparison to the SMA displacements, HRGP time-series are very useful since important waveform features can be observed over the same time window as SMA data. Avallone et al. (2016) provides time-series for 52 stations with sampling rates from 1 to 20 Hz. The time-series were processed using two different software packages (GAMIT and GIPSY) and are freely available (ftp://gpsfree. gm.ingv.it/amatrice2016/hrgps/solutions/20160824/). For this paper, only the "GD2P" (GIPSY) time-series will be considered since it was shown that there is negligible difference between the two approaches (Avallone et al. 2016). Time-series are available for AMAT (10 Hz), ASC0 (1 Hz), ASCC (1 Hz), LNSS (1 Hz), NRCI (1 Hz) and MTER (10 Hz) stations will be used for comparison to the consensus and SMA displacement results. Table 2 lists the GPS stations, nearest SMA site and distance between them.

InSAR data can help to fill gaps in the GPS and SMA coverage and obtain displacement trends. Data from the European Space Agency satellites Sentinel 1A/B are available in the form of interferograms and phase unwrapped decomposed solutions. The decomposed solutions provide quasi up-down and quasi east–west displacements from the data of the ascending and descending tracks of 1A/1B (Marinkovic and Larsen 2016), available at https://zenodo.org/record/61133. The availability of the decomposed solution in GeoTiff format allows the displacements to be determined for any GPS coordinate in the coverage area. Japan Aerospace Exploration Agency operates the Advanced Land Observing Satellite 2 (ALOS-2) which has also mapped the coseismic displacement during this event. The ascending and descending tracks of ALOS-2 have been decomposed into quasi up-down and quasi east–west displacement components (GSI 2016). However, this data is only available in.png and. kmz overlay thus the Sentinel 1A/B decomposed solution will be considered in this study. Both decomposed solutions show a peak subsidence of ∼ 20 and ∼ 20 cm of peak east–west movement. An important note on the InSAR coseismic displacements is that they capture a much larger time window than SMA, like the consensus GPS offsets. Sentinel 1A/1B results represent the displacement from 21 to 27 August for both the ascending and descending tracks (ESA 2017). The ALOS-2 data has a larger temporal window with nearly one year on the ascending track and three months on the descending track (GSI 2016). Therefore, a match on the displacement magnitudes between

Table 2 GPS, SMA distance and InSAR/GPS displacements for E/W and U/D components

| GPS (SMA)	Dist. (km)	East (cm)		Up (cm)	
		GPS	InSAR	GPS	InSAR
AMAT (AMT)	0.8	− 1.1	− 1.6	− 1.5	− 4.4
ASCC (ASP)	4.6	1.3	–	− 0.2	–
ASC0 (ASP)	3.5	1.5	–	− 0.1	–
LNSS (LSS)	7.7	− 1.7	− 1.9	0.4	1.2
NRCI (NOR)	0.07	− 2.2	− 3.9	0.5	5.8
NRCI (NRC)	0.27	− 2.2	− 3.9	0.5	5.8
MTER (RM33)	Collocated	− 0.2	− 0.4	0.1	0.1

SMA, InSAR and GPS consensus is not always obtained. Table 2 compares the GPS consensus and InSAR displacements for the Up and East components. The directions are always consistent, but the magnitudes do not match, especially for the Up component. This underscores the uncertainty in determining the residual displacement from SMA since there is even significant variability across the comparable displacement data. Hence, residual displacements obtained from SMA data must be considered approximate.

2 Residual displacement from SMA data

The current widespread usage of digital instruments has made it possible to extract residual displacement from accelerometric data. Digital instruments generally provide superior low frequency sensitivity compared with their analog counterparts. However, the digital recordings often still contain low frequency signal contamination which may be attributed to instrument noise, zero baseline shifts and tilt (Boore and Bommer 2005). The presence of instrument noise can be ascertained by examining the signal to noise ratio (SNR) by using the recording from the pre-event portion of the acceleration time series. If the instrument noise is low, SNR ≥ 3 (Boore and Bommer 2005), then low frequency contamination can be attributed to either zero baseline shifts or tilt. Ironically, Iwan et al. (1985) has observed that zero baseline shifts can occur on a digital instrument, due to transducer hysteresis, at relatively low level of acceleration ($\sim$ 50 cm/sec^2). If ground tilting occurs during the seismic event, the instrument is no longer recording along a true horizontal or vertical axis.

Part of the low frequency content of the signal may result from the residual displacement in near-field records. If the cause of the low frequency signal is residual displacement, it acts to modulate the higher frequency displacement components. It has been well established in the literature that these low frequency components manifest with sinusoidal accelerations which integrate to dominant single sided velocity pulses. After integrating again, the displacement resembles a "fling" or step-like waveform (Makris and Chang 2000). Acceleration time histories that double integrate to non-zero displacement at the end of the record can be called residual displacement ground motions (RDGM). RDGM are generally not distributed by ground motion providers and databases. This is because their processing methodologies involve the use of standard high-pass or band-pass filtering which removes both the low frequency contamination and the low frequency signal attributed to the residual displacement (Paolucci et al. 2011; Pacor et al. 2011; Boore et al. 2012). As a result, researchers have proposed schemes to recover RDGM by different techniques to retain the low frequency signal responsible for residual displacement but discard the noisy portion. Research has shown (Yang et al. 2017) that the inclusion of RDGM is important for the engineering design and analysis of fault crossing infrastructure such as bridges and tunnels.

Baseline offsets from tilting or other mechanisms manifest as linear acceleration or velocity trends. Graizer (1979) was perhaps the first attempt at a method to recover RDGM. He used a polynomial correction scheme in conjunction with constraints on the sum of squares of the adjusted velocity time series. The method of Iwan et al. (1985), with modifications, is perhaps the most widely used by researchers. Iwan et al. (1985) suggested using two constant acceleration adjustments, a_m over the time from t_1 to t_2 and a_f over the time from t_2 to t_f, to correct for linear velocity trends (see Fig. 2). This method was based on the response of the PDR-1 accelerograph and FBA-13 transducer during laboratory
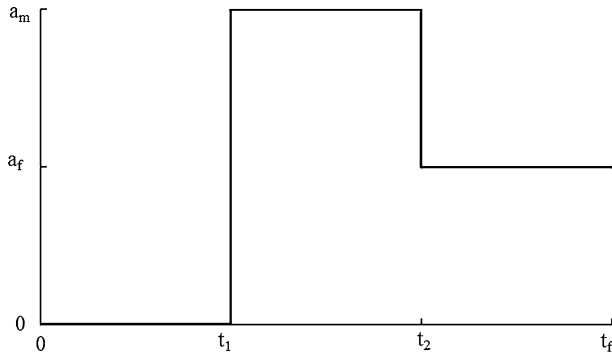
Fig. 2 Acceleration versus time of Iwan et al. (1985) correction

testing. Therefore, some of the recommendations in Iwan et al. (1985), such as time instant selection based on a threshold acceleration (50 cm/sec^2) and the need for two linear corrections are based specifically on the response of the sensor studied. The same behavior is not expected for other digital sensors and the correction must be evaluated on a case-by-case basis. As a result, subsequent researchers have added necessary modifications to the method, a few of which will be discussed here.

One of the difficulties in applying two linear corrections is determining the time instants for such correction. It has been shown that the displacement results are sensitive to the time instant selection (Boore 2001). For some recordings, two linear baseline drifts may be observed in the velocity trace while for others only a single linear offset is obvious. Numerous modifications have been investigated to reduce the level of subjectivity in selecting the time instants, including those by Boore (2001), Wu and Wu (2007), Akkar and Boore (2009), Chao et al. (2010), and Rupakhety et al. (2010). Boore (2001) proposed the "v0 correction" which finds t_2 using the time when a line fit to a portion of the raw velocity waveform becomes zero. This constraint helps to remove the subjectivity in determining t_2. However, the determination of t_1 is still subjective and the displacement results were sensitive to the selection. Akkar and Boore (2009) considered 4 different acceleration baseline offset models with Monte Carlo simulations to generate a suite of corrected waveforms for some records of the 1999 Chi–Chi earthquake. The suite of ground motions was used to obtain an average for comparison to GPS data and response spectrum analysis. Their simplest model (M1) used a single constant acceleration offset (single linear velocity correction) and produced results which compare well to the average of the entire Monte Carlo simulations. Simple baseline offset models like this will be considered in this paper. Rupakhety et al. (2010) contains a thorough review of the relevant modifications to the original Iwan et al. method and introduced their own. Selection of t_2 in their study of Iceland's ICEARRAY ground motions was based on the flatness of the low frequency portion of the Fourier amplitude spectrum of velocity. In the same study, t_1 was selected as the p-wave arrival time to reduce the subjectivity.

In this study, the residual displacement waveforms resulting from two methods will be used. The first method relies on low pass filtering to identify and retain the velocity pulse responsible for the residual displacement (Method 1). The second method applies a single linear drift correction using regression on the velocity or displacement time series to remove the baseline offset (Method 2). Method 2 can be considered a modification of the Iwan et al. procedure where the selection of time instants is not subjective since it is based

on minimizing the sum of the square of the velocity. Instead of two linear corrections, only one is applied since the waveforms do not show evidence of the need for two linear corrections. Using two different methods gives additional confidence in the results when there is agreement. There is always considerable uncertainty when extracting residual displacements from the SMA data, even when there are nearby GPS stations for comparison. Both methods take all adjustments back to the acceleration time series which allows integration to velocity and displacement using zero initial boundary conditions and ensures compatible time series. The RDGM time series presented in this work for Method 1 are available in the electronic supplement of this paper.

3 Fourier analysis of the accelerometric data

Before processing the acceleration time series to extract the RDGM, the frequency content of the raw data is reviewed. Method 1, which will be discussed in Sect. 4, identifies the dominant velocity pulse from lowpass filtering and is most effective when this signal contains only the velocity pulse and baseline offset. Therefore, a high SNR in the low frequency range is desirable for this method. Although Method 2 does not explicitly examine the frequency content of the record, the linear regression can be adversely affected by a noisy recording since the "quiet" portions of the velocity and displacement traces would contain long period transients. Processing of the time series before the Fourier analysis is limited to removal of the mean of the pre-event portion ($\sim$ 5–6 s for most records, $\sim$ 60 s for RM33) from the entire record. The relatively short pre-event record on most stations is not ideal and longer pre-event times are preferred for greater accuracy in the low frequency spectrum. SNRs are generally high in the low frequency range, which can be seen on Fig. 3. Instrument noise can be considered negligible when SNR $\geq$ 3 $\approx$ 4.8 dB (Boore and Bommer 2005). One exception is the Up component of RM33 (Fig. 3g) where the SNR drops to 3.3 dB over the frequency range 0.01–0.02 Hz. It can be seen from Fig. 3g that the North component of the RQT station is compromised, however the East and Up components are reasonable from a SNR perspective.

The test for tilting per Graizer (2010) has been performed by examining the horizontal to vertical Fourier spectrum ratios (HVR) of the six SMA sites examined in this paper (RQT is excluded due to incomplete triaxial recording). Since horizontal components are more sensitive to tilting than the vertical component, and in the absence of tilt the horizontal and vertical components are expected to have comparable low frequency content, the low frequency HVR is inspected for an order of magnitude (10 dB) gain. If the HVR $\geq$ 10 dB, then the low frequency content may be attributed to tilting otherwise it may be attributed to residual displacement. HVR for North and East components are shown in Fig. 4. The six near-field stations are shown (dotted), along with their average (heavy line), and the average of three far-field stations, ANB, CER, and VITU (heavy dashed). The three far-field stations have $R_{epi} \approx$ 100, 200 and 300 km, respectively. Far-field stations are selected for comparison to the near-field stations due to the expected absence of both residual displacement and tilting. According the HVR criteria, only the LSS station exceeds 10 dB, and only for a small frequency range. Therefore, according the criteria of Graizer (2010), tilt is not expected to have influenced the recordings in general. Further evidence can be seen from the far-field recordings which exhibit similar peak gains compared to the near-field records at slightly higher frequencies. Since the far-field
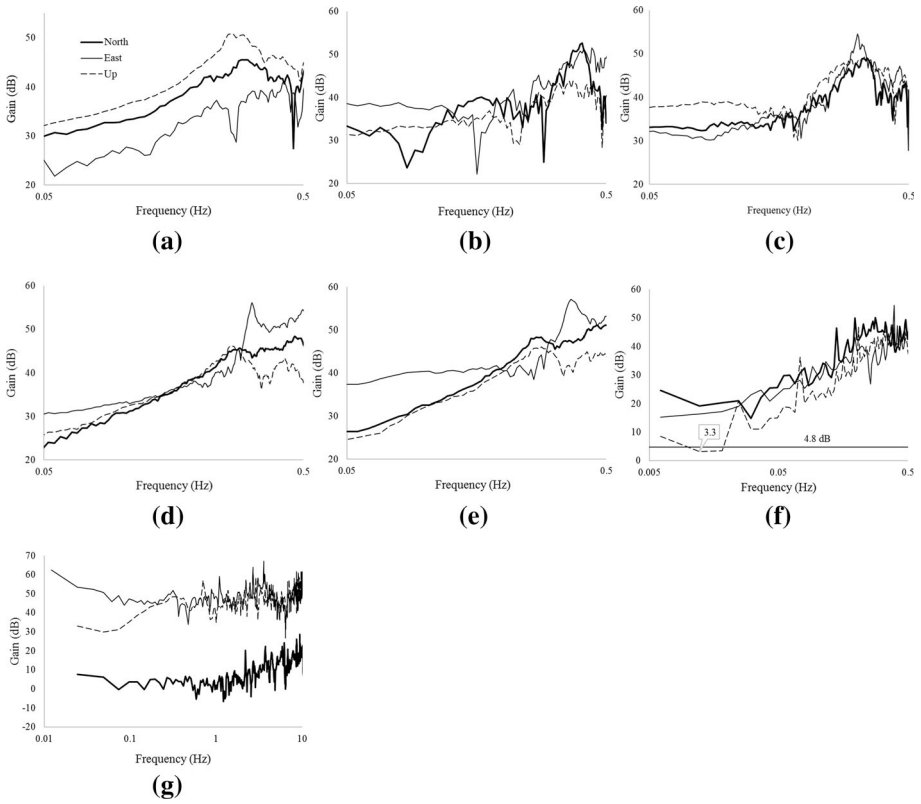
Fig. 3 SNR for all stations. **a** AMT. **b** ASP. **c** LSS. **d** NOR. **e** NRC. **f** RM33. **g** RQT
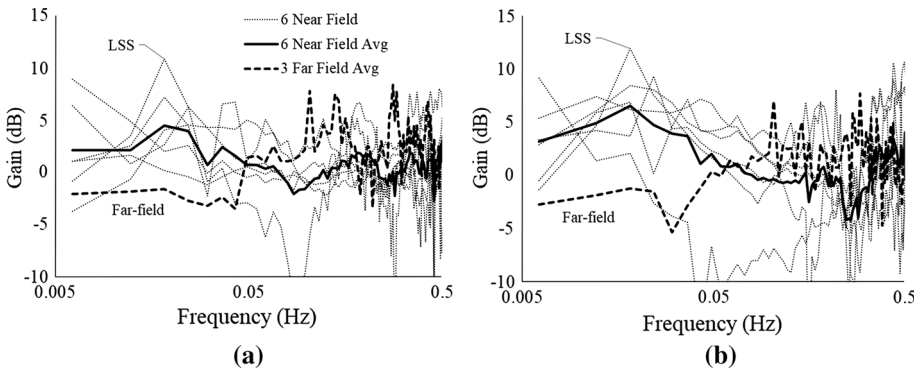
Fig. 4 HVR for near-field and far-field recordings. **a** North. **b** East

recordings should not be affected by tilting, these localized peaks in the near-field HVR can likely be attributed to the frequency content or residual displacement but not tilt.

4 Velocity pulse identification: method 1

This method relies on low pass filtering to identify a dominant velocity pulse in the low frequency content. It has been shown that the instrument noise is low for the stations investigated in this paper as discussed in Sect. 3. Using an acausal Butterworth (4th order) filter a zero baseline time series (a_0) can be generated by either a high pass filter to remove only low frequency content (a_{LF}), or a bandpass filter which removes both low and high frequency (a_{HF}) content. The zero baseline time series can be expressed by Eq. 1, for the case where a high pass filter is used (Trifunac 1971).

$$a_0(t) = a_{raw}(t) - a_{LF}(t) \tag{1}$$

Next, a low pass filter with the same low frequency corner (f_c) used to generate a_0 is used to obtain the low frequency time series which was removed (a_{LF}). After integration to velocity (v_{LF}), this time series contains both the baseline offset and a dominant velocity pulse. Using v_{LF}, the portion belonging to the baseline offset will be discarded and the velocity pulse retained. From a physical standpoint, baseline drifts do not oscillate and will diverge from the zero line, so v_{LF} is retained until the last zero crossing and denoted as the "step" time series (v_{step}). The corner frequency is selected by matching the dominant velocity pulse to the Type A pulse (Makris and Chang 2000), based on least squares residual. The Type A velocity pulse depends on the pulse period (T_P) and peak velocity (V_p) and is expressed by Eq. 2. When finding the Type A pulse parameters, V_p is matched to the peak from v_{step} and the pulse period is determined from the zero crossings before and after the peak. Once f_c is found, the corresponding acceleration time series (a_{step}) is added to a_0 to generate the adjusted acceleration (a_{adj}). The adjusted acceleration can be expressed by Eq. 3 and is devoid of baseline offsets and contains a dominant pulse which will integrate to residual displacement.

$$\dot{u}_g(t) = \frac{V_p}{2} - \frac{V_p}{2}\cos(\omega_p t) \quad 0 \le t \le T_p \tag{2}$$

where V_p = peak velocity, $\omega_p = 2\pi/T_p$, T_p = Pulse Period.

$$a_{adj}(t) = a_0(t) + a_{step}(t) \tag{3}$$

The Lucerne Valley record (N90E and N00E components) of the 1992 Landers earthquake is now considered. This time series has already been de-noised by Iwan and Chen (1994) and results in residual displacement for both components as shown on Fig. 5a, b.

The dominant velocity pulse for both components is shown on Fig. 6c, d, where the dashed line shows the matching Type A pulse and the solid line is v_{LF}. The low pass time series is retained until the last zero crossing, now called the "Step" time series, and added back to the zero baseline time series to generate the adjusted displacement shown in Fig. 6a, b. Various corner frequencies are shown on Fig. 7a, b to illustrate the effect of its selection, which is minimal. For this record the chosen frequency based on least square residual to the Type A model are 0.055 and 0.062 Hz for the North and East components, respectively. These results represent the target criteria for the time series after removing the baseline offset: a dominant single sided velocity pulse followed by only oscillatory motion.

The method is now applied to the raw North and Up components of the TCU052 record from the 1999 Chi–Chi earthquake which have not been de-noised already. This time series has been used by various researchers including Akkar and Boore (2009), Rupakhety et al.
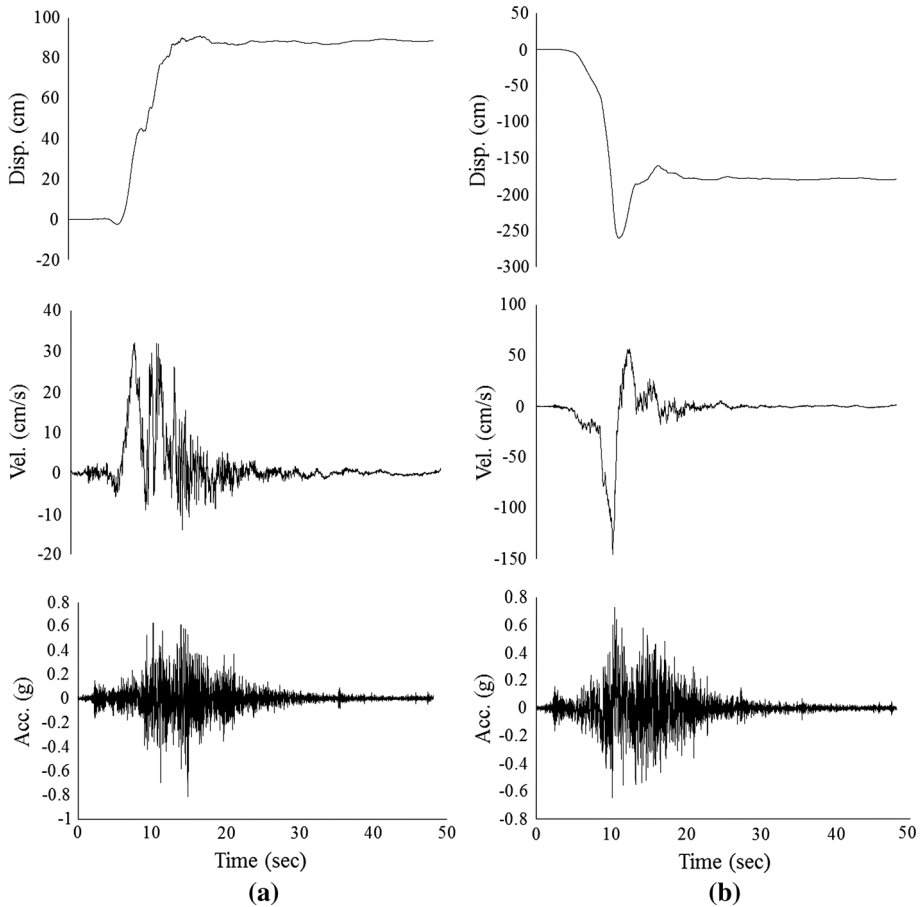
Fig. 5 Lucerne valley time series. **a** North Component. **b** East Component

(2010), Wu and Wu (2007), and Chanerley et al. (2009). GPS offsets are also available for comparison. Results for Method 1 and Method 2 (discussed later) are presented on Fig. 8 along with the results from GPS and other researchers. There is good agreement between the final displacements using Method 1 and those obtained by other researchers. The selected corner frequencies are 0.0585 Hz (Up) and 0.054 Hz (North). The velocity pulse is shown on Fig. 9 for both components. The baseline drift is obvious for both components after t ≈ 25 s from the low pass time series. The matching Type A pulse is also shown on Fig. 9 along with the step time series which is retained to generate the residual displacement component.

5 Linear velocity and displacement adjustments: method 2

Observing the raw velocity and displacement waveforms from the 24 August 2016 earthquake, linear trends are present in both the velocity and displacement waveforms. There does not appear to be an obvious need for multiple linear adjustments per Iwan et al.
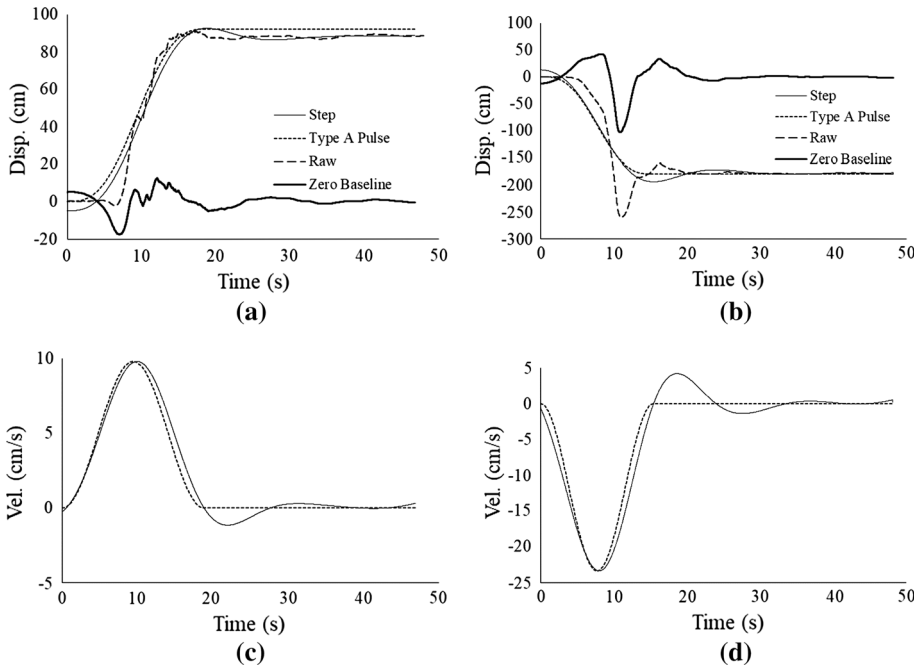
Fig. 6 Lucerne valley—Method 1. **a** North Component—Disp. **b** East Component—Disp., **c** North Component—Vel. Pulse. **d** East Component-Vel. Pulse
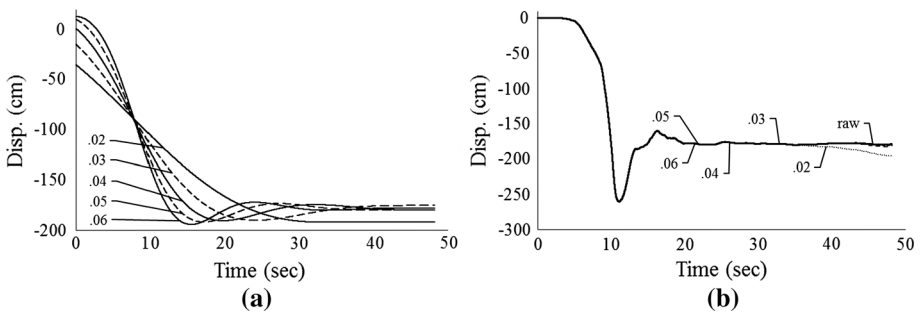

Fig. 7 Effect of corner frequency—Method 1. **a** Step Disp.—Last Zero Crossing. **b** Adjusted Disp.—last zero crossing

(1985), instead either a constant acceleration or velocity offset is used which extends from t_1 to the end of the record t_d. Most of the earlier research (Iwan et al. 1985; Boore 2001; Wu and Wu 2007) was focused on adjusting linear velocity drift, however linear displacement drift has also been observed. Adjustment procedures are proposed to remove both types of drift. For the drift models used in this paper, there is no subjectivity in the selection of t_1 and the procedure is semi-automatic. The only judgement to be made is whether the velocity or displacement has a linear trend, which is easily observed from the raw displacement. However, the author is testing a larger ground motion database to determine an automation algorithm for this selection. In addition, it is noted that larger
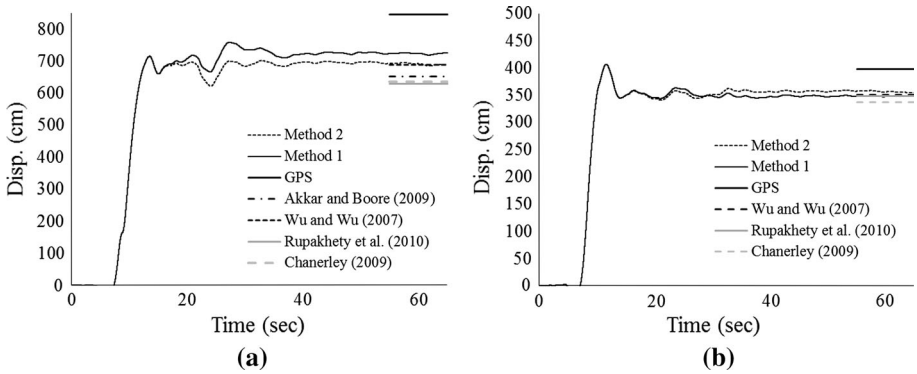
Fig. 8 TCU052—adjusted displacements north and up components. **a** TCU052- North. **b** TCU052- Up
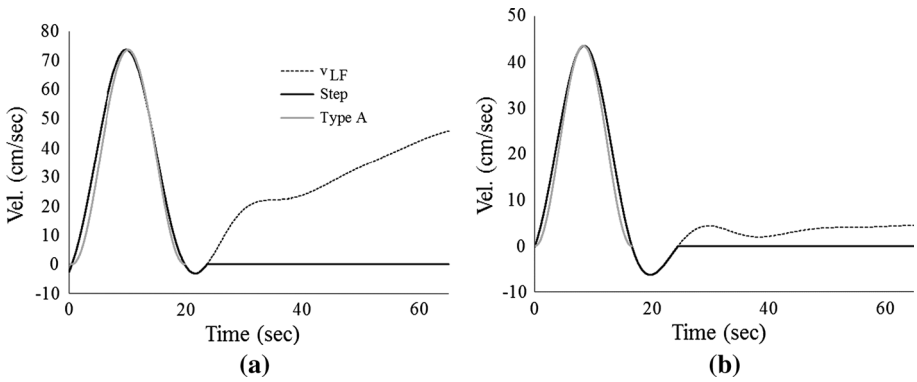
Fig. 9 TCU052—velocity pulse North and up components. **a** TCU052- North. **b** TCU052- Up

magnitude events, or stations closer to the ruptured fault may require multiple segment linear adjustments.

5.1 Linear velocity adjustment

The adjustment for linear velocity drift is made in accordance with the time series on Fig. 10a. While other researchers have used the derivative of the linear velocity regression to make the acceleration correction, I have instead used a different version based on the resulting numerical integral, although in most cases the difference is likely negligible. A linear regression is fit to the raw velocity time series from time t_1 to t_d. The linear regression equation for velocity is given by Eq. (4), with coefficients v_1 and v_0 found by least squares regression.

$$v_{fit}(t) = v_1 t + v_0 \tag{4}$$

The constant acceleration adjustment (a_c) is found by Eq. (5) based on the numerical integration of the acceleration shown in Fig. 10a with the total velocity adjustment equal to v_f. The velocity adjustment (v_f) is obtained by the difference in the regression equation (Eq. 4) evaluated at t_d and t_1.
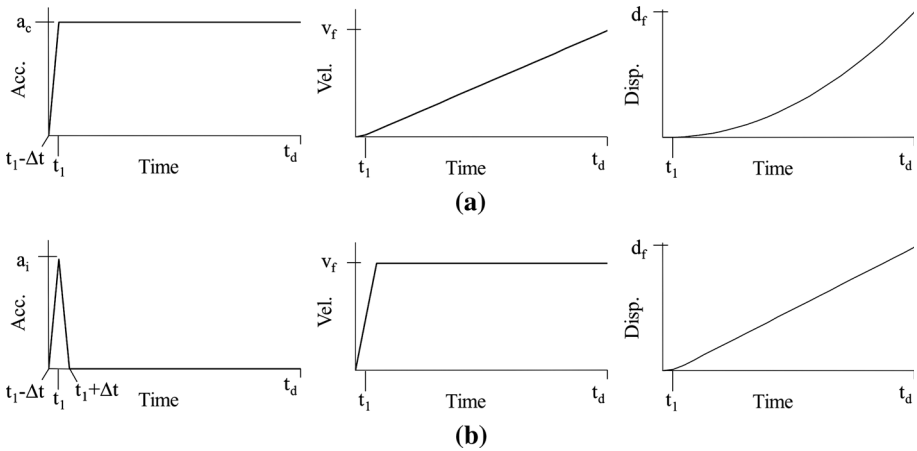
Fig. 10 Time series for adjustments. **a** Linear velocity adjustment. **b** Linear displacement adjustment

$$a_c = \frac{v_f}{\left(t_d - t_1 + \frac{\Delta t}{2}\right)} \tag{5}$$

The adjusted acceleration is found by subtracting the acceleration time series of Fig. 10a from the raw acceleration. Finally, the adjusted velocity (v_{adj}) and displacement are obtained by integration.

To remove the subjectivity in the time instant selection, t_1 is found by minimizing the sum of the square of the adjusted velocity. In this paper, the t_1 selection criteria can be expressed by Eq. (6), where t = 0 is taken as the end of the pre-event noise (p-wave arrival).

$$t_1 \sum \min \left\{ \int_0^{t_d} \left[v_{adj}(t) \right]^2 dt \right\} \tag{6}$$

Graizer (1979, 2010) has previously suggested using the sum of the square of the velocity over a quiet portion at the end of the record. I have investigated this criterion as well, and have found that the results are generally comparable to the approach taken here. Although there are certain cases where the resulting waveforms using Graizer's criteria are completely unphysical due to the bias placed on the end velocity. For other noise models (multiple linear drifts, etc.) this may be more appropriate than for the single linear drift model. This could be corrected by limiting the selection of t_1 to a certain interval determined by inspection of the raw waveforms. Since this introduces subjective criteria, it has not been considered.
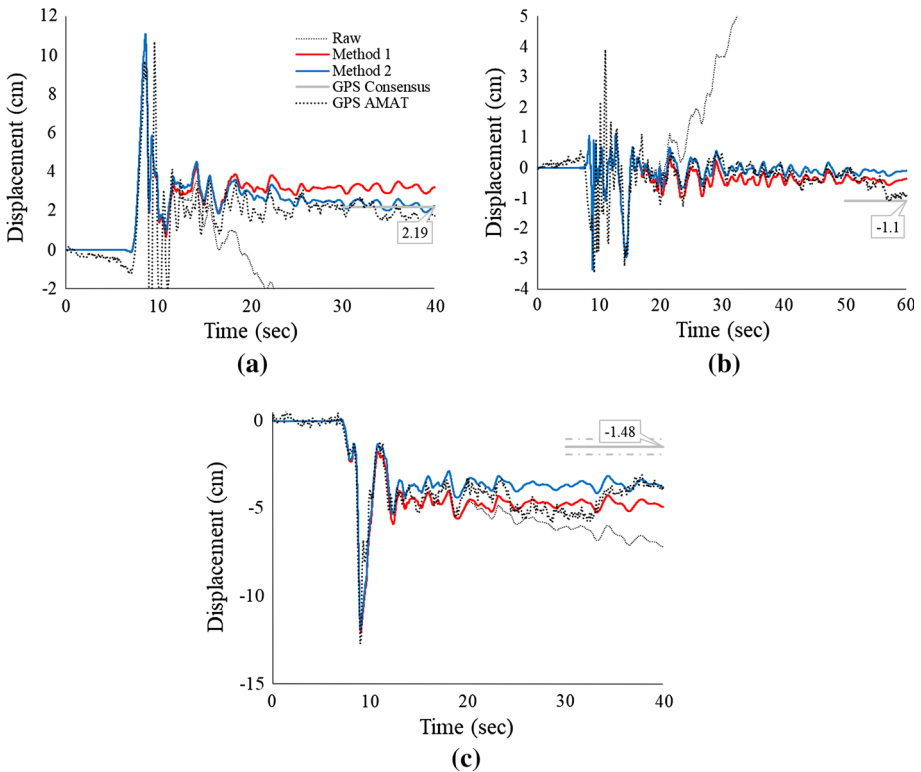
5.2 Linear displacement adjustment

To correct for linear displacement drift, an acceleration impulse is used to generate a constant velocity offset. Waveforms used for this adjustment can be observed from Fig. 10b. The impulse applied at t_1 results in approximately constant velocity and linear displacement. Linear regression is performed again, except on the raw displacement time series, to generate d_{fit} using a similar form to Eq. 4.

The impulse a_i (Eq. 7) is calculated using numerical integration of the Fig. 10a waveforms, with total displacement adjustment equal to d_f. The value of d_f is found by taking the difference of the regression function at time t_d and t_1.

Table 3 Summary of Method 1 and Method 2 parameters

	Method 1			Method 2						
	North	East	Up	North		East		Up	
	f_c (Hz)	f_c (Hz)	f_c (Hz)	V or D	t_1	V or D	t_1	V or D	t_1
AMT	0.073	0.047	0.075	V	7.73	V	16.925	D	6.985
ASP	0.065	0.065	0.048	D	18.625	D	21.105	D	20.22
LSS	0.06	0.08	0.1	D	20.6	D	25.785	D	19.8
NOR	0.055	0.05	n/a	V	10.46	V	10.325	n/a	n/a
NRC	0.099	0.105	0.08	V	11.625	V	13.505	V	5.765
RM33	0.08	0.054	0.03	V	11.825	V	9.395	V	14.22
RQT	–	0.082	0.083	–	–	–	–	D	8.78

Fig. 11 AMT displacement. **a** North. **b** East. **c** Up
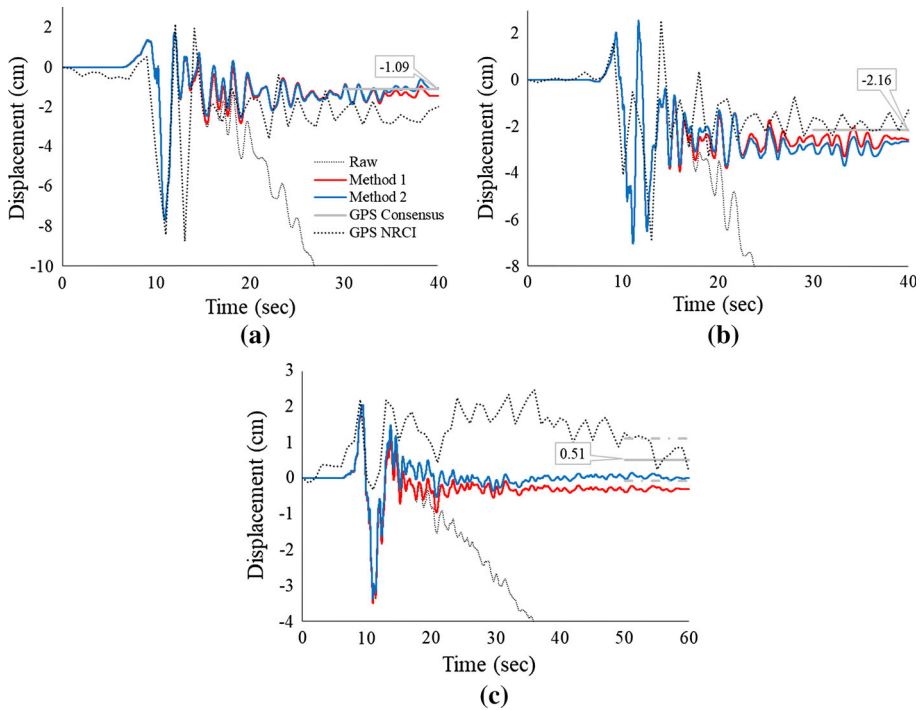
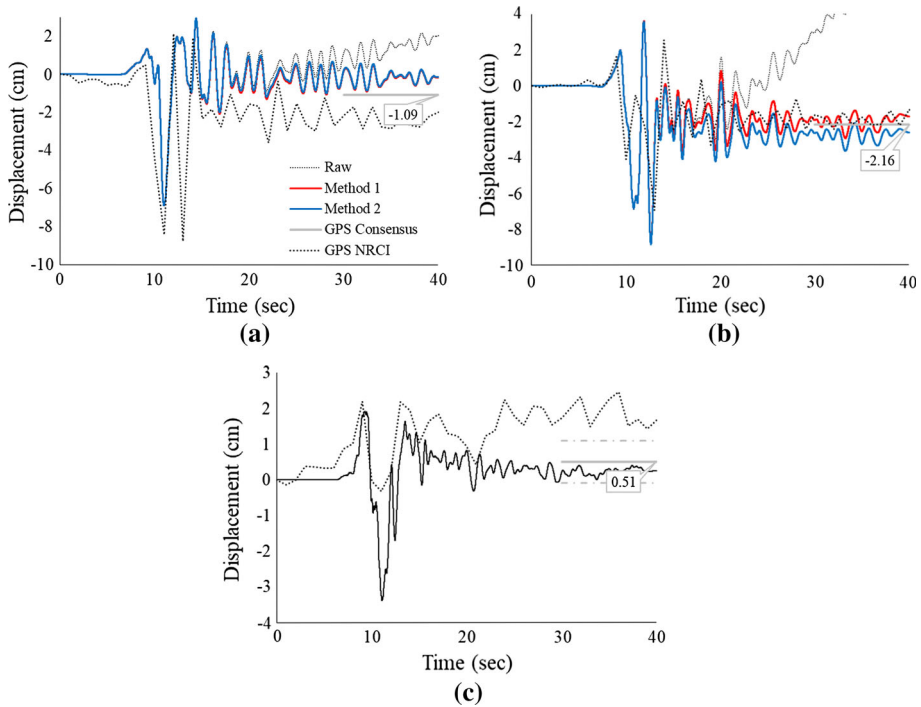Fig. 12 NRC displacement. **a** North. **b** East. **c** Up

$$a_i = \frac{d_f}{\Delta t(t_d - t_1)} \tag{7}$$

Once the acceleration adjustment is made, the adjusted velocity and displacement are found by integration. Selection of t_1 uses the same criteria as Eq. 6.

Figure 8 contains the results for the TCU052 recording from 1999 Chi–Chi earthquake. The Method 2 results show comparable waveforms to both Method 1, and final displacements matching well to other researchers and GPS. Both Up and North components required a linear velocity adjustment based on observation of the integrated raw waveform. For the Up and North components, the time instants are $t_1 = 13.32$ s and $t_1 = 14.225$, respectively.

6 24 August 2016 Amatrice results

The results for the SMA stations from the 24 August 2016 Amatrice event are now considered. Table 3 lists the parameters based on the Method 1 and Method 2 procedures for the stations considered. Figure 1 contains a comparison of the horizontal displacement vectors obtained from the SMA (Method 2) and GPS offset data. In general, Fig. 1 shows good agreement on resultant direction and magnitude between both sets of data. Some basic processing is performed on the recordings before Method 1 and Method 2 procedures are applied. This is limited to subtracting the mean of the pre-event portion from the entire record and application of a 5% cosine taper. In the case of RM33, the pre-event portion was

Fig. 13 NOR displacement. **a** North. **b** East. **c** Up

also truncated due to its long length. Figures 11, 12, 13, 14, 15, 16, 17 and 18 contain the displacements obtained from Method 1, Method 2, Consensus GPS offsets, GPS waveforms, and InSAR (where applicable) along with the raw time series. In general, 40 s of data is presented due to the presence of early aftershocks occurring shortly afterwards and adequately captures the strong motion window. For the recordings in Amatrice, results are shown on Fig. 11. Referring to Fig. 11a, the North component for Method 2 has good agreement between the adjusted SMA data, 10 Hz GPS waveform at AMAT and the consensus offset. From Fig. 11b the same good agreement can be seen until t ≈ 50 s, thereafter the AMAT waveform takes an unexpected downturn. As a result, the final displacement magnitudes do not match well. This time series is extended to 60 s to illustrate this effect and the reason why the consensus offset is not in good agreement. In fact, the same behavior can be seen on Fig. 11c. Although the SMA data matches well to the GPS waveform on Fig. 11c, the GPS and SMA waveforms have about 2 cm greater subsistence than the consensus offset. The dash-dot lines above and below the consensus offset indicates the uncertainty range. In this case, both Method 1 and Method 2 are beyond the lower bound of the consensus offset, but match better to the GPS waveform. This GPS station is located on the top of a building and not in the free field, thus the building response may be a contributor to the behavior seen on the GPS waveform (Avallone et al. 2016).

Figures 12 and 13 contain the waveforms for NRC and NOR, respectively, located in Norcia. The same waveform features can be seen from both SMA records. It can be seen from Figs. 12a/13a that Method 1 and 2 provide matching waveforms. Although the GPS sampling rate is only 1 Hz, it has similar features to the SMA data: an initial spike towards
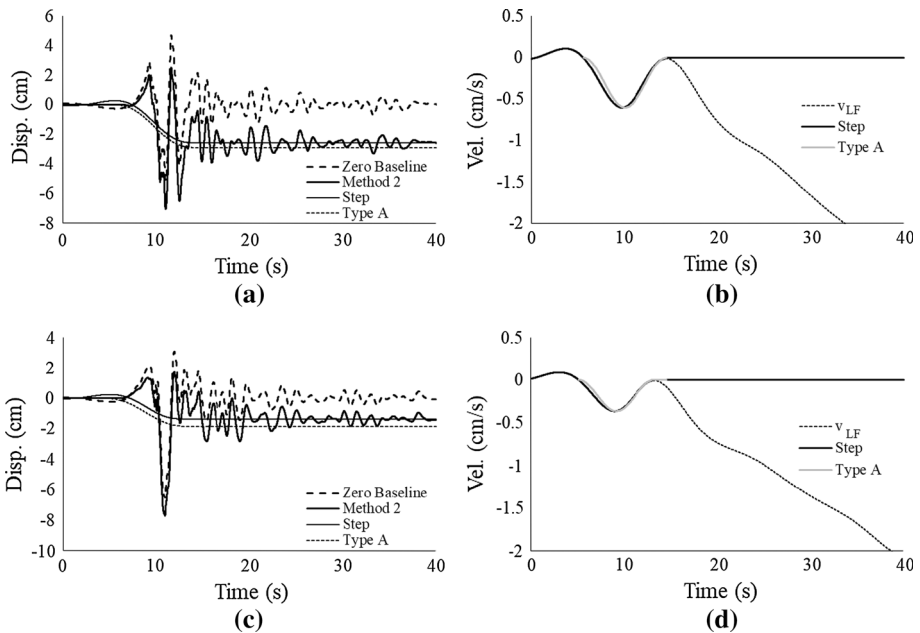
Fig. 14 NRC method 2 Time Series. **a** East—displacement. **b** East—velocity. **c** North—Displacement. **d** North—velocity

the south with a subsequent retracement back to ~ -2 cm. One difference between the GPS and SMA waveforms is the lack of a second spike toward the south about 2 s after the initial spike and with matching magnitude ~ -8 cm. The lack of this second spike on the SMA records may possibly be due to convolution or that the NRCI GPS station is installed on top of a building (Avallone, et al. 2016). Figures 12b/13b match the East component of the GPS waveform and the consensus offset well, with NOR matching slightly better than NRC. For the Up component shown on Fig. 12c, the final adjusted SMA data is within the uncertainty of the consensus GPS data. However, the waveform features are difficult to compare due to the higher frequency behavior on SMA which cannot be captured well by the 1 Hz GPS. The NRCI Up waveform features at the beginning of the record (between $t \approx 8$ to 10 s) do compare well to the SMA data with an initial spike up, retracement down, then ultimately back up to its residual value. The Up component of NOR (Fig. 12c) was not adjusted since it's integrated raw form does not show baseline drift. Figure 14 contains the plots for Method 1 results from the North and East components, like those shown for Lucerne Valley and TCU052 on Figs. 6 and 9. The extracted single sided velocity pulse is clearly visible along with the baseline offset which is removed.

The SMA to GPS distance is < 1 km for the Amatrice and Norcia sites, but those from Leonessa (LSS) and Ascoli Piceno (ASP) are a bit further in the range of 3.5–7.7 km (Table 2). From Fig. 15, the waveform features from LSS and GPS LNSS match well. The final displacement values for all components are lower in magnitude than the GPS waveform and consensus results, although the East component matches well to InSAR. The Up component (Fig. 15c) was not adjusted because there is no baseline drift, and it lies just outside of the uncertainty of the GPS consensus. The LNSS waveform for the East and Up component contains relatively large displacement prior to the arrival of the p-wave
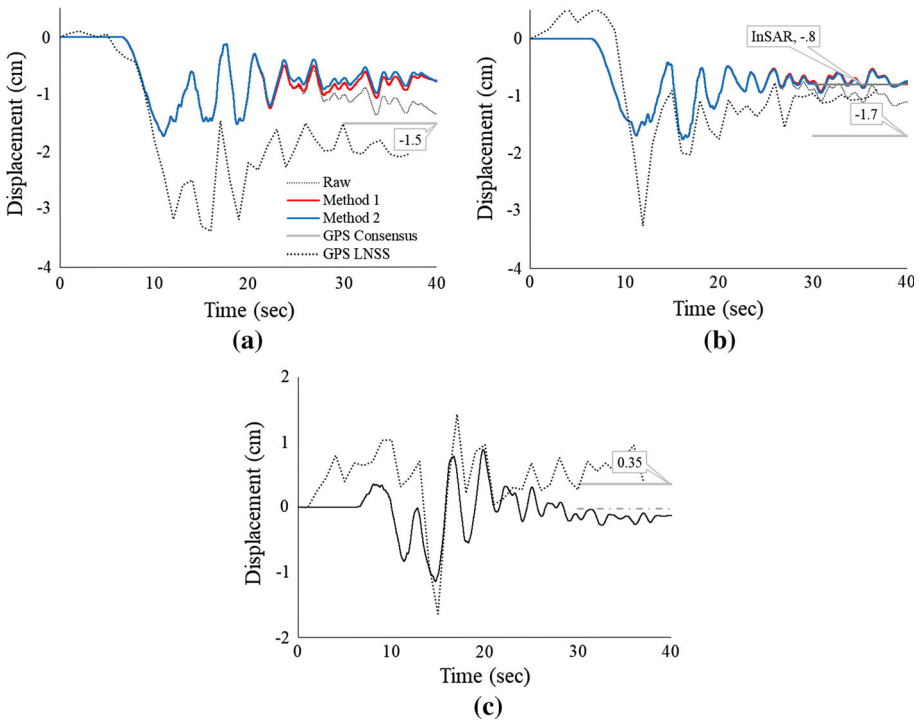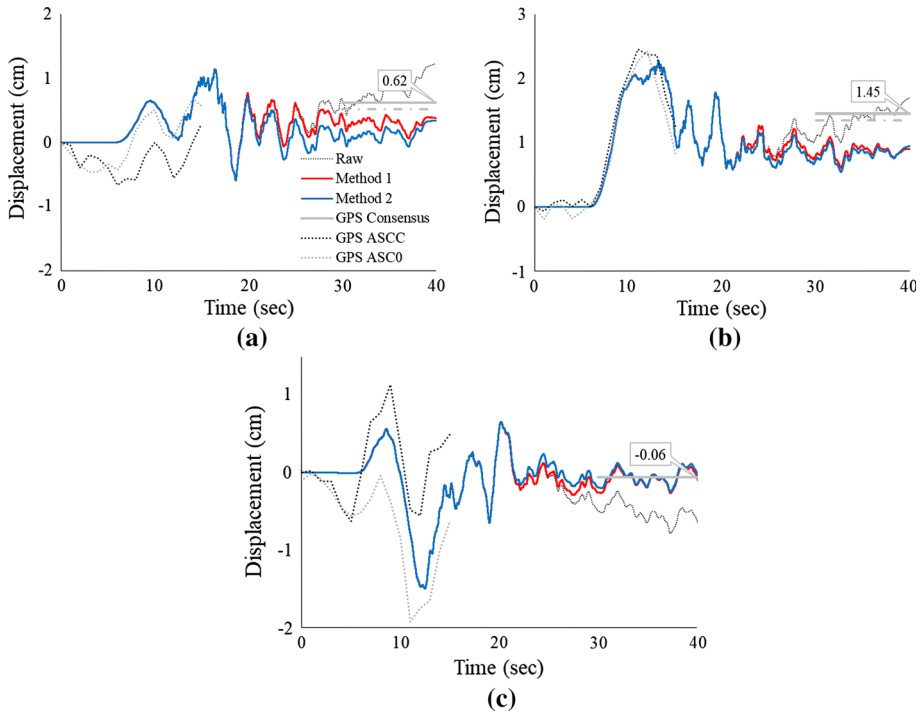
Fig. 15 LSS displacement. **a** North. **b** East. **c** Up

($\sim$ 1 cm), which could possibly be removed by processing the GPS waveform. For this paper, the only processing was to zero the GPS waveform at t = 0 on the SMA record.

For the Ascoli Piceno stations ASP (SMA), ASC0 (GPS) and ASCC (GPS), waveforms are shown on Fig. 16. There was a power outage at the GPS site which explains the sudden cessation of data at t $\approx$ 15 s. It is obvious that there is good agreement at the beginning of the record for all three components between the SMA and GPS waveforms. Final magnitudes are in good agreement for the North and Up components, while the results from Method 1 and 2 underestimate the displacement in the East component compared to the GPS consensus. The final displacements match better than for LSS, which is probably due to the closer proximity of the SMA and GPS. InSAR data is not available for comparison since this location is outside of the coverage zone of the Sentinel results.

Figure 17 contains the waveforms for the SMA station RM33 and MTER (GPS). Although the displacements are all less than 1 cm, this site is of interest since the SMA and GPS sites are collocated. Excellent agreement can be seen between the waveforms, consensus GPS and Method 1 and Method 2 results, particularly during the first 40 s. The time series has been extended to 60 s to again show the presence of some spurious GPS waveform features which have been seen at other sites. The MTER GPS waveform shows a long period transient between about 30 and 60 s for all components. The instrument noise on the SMA Up component does not seem to have negatively impacted the results for either method.

RQT station (Fig. 18) has been investigated due to its proximity to the epicenter, even though there is no comparable GPS station, so InSAR displacements are used. The North
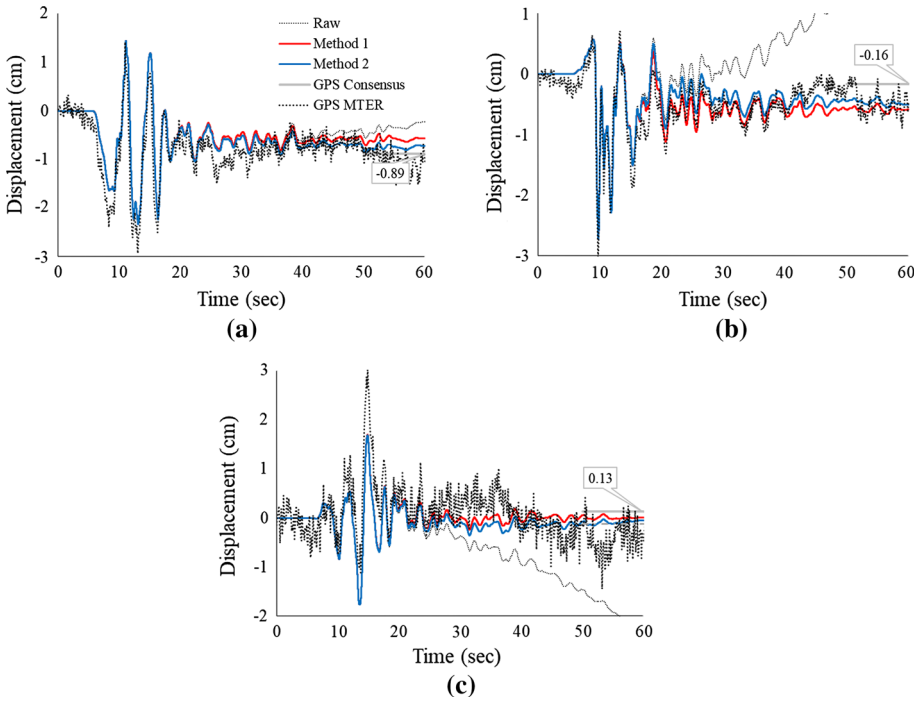
Fig. 16 ASP displacement. **a** North. **b** East. **c** Up

component is not a reliable signal and has not been considered. The Up component was adjusted using the same procedure for Method 1 and Method 2 with comparable waveforms which result in lower final displacements than InSAR. The Up waveforms resemble those from AMT, NRC and NOR except with larger residual displacement. For the East component (Fig. 18a), the resulting Method 1 waveform appears unphysical which is attributed to noise at 0.4 Hz frequency. Thus, the results were high pass filtered (f_c = 0.4 Hz) beyond t = 12.53 s to remove the noise. The resulting waveform is indicated as "Method 1 + HP". Method 2 results are not presented because this additional noise yielded poor results.

7 Conclusion

Two methods have been considered to extract RDGM from the near-field SMA recordings of the 24 August 2016 earthquake. Method 1 uses acausal filtering to extract the low frequency component, remove baseline offsets, and select the corner frequency by matching the dominant velocity pulse to the Type A analytical pulse model. Method 2 uses modifications to the existing method by Iwan et al. (1985) to remove a single constant baseline offset in either acceleration or velocity. There is no subjectivity in selecting the time instant t_1. Comparing the results to ground motions from 1999 Chi–Chi which have been heavily researched by others, these two methods provide waveforms consistent with the previous results. From the results presented for the SMA sites with comparable GPS

Fig. 17 RM33 displacement. **a** North. **b** East. **c** Up
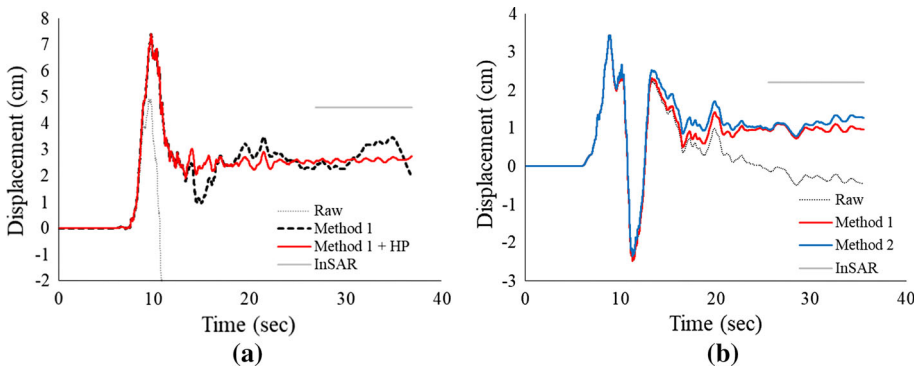
Fig. 18 RQT displacement. **a** East. **b** Up

data, it has been shown that Method 1 and Method 2 provide similar waveforms. These adjusted time series compare well to the GPS waveforms and consensus data in most cases. Results for the RQT station are also presented although there are no nearby GPS results to compare, so the InSAR displacements are used instead. The methods presented in this paper are effective in removing linear velocity and displacement trends. Since the selection criteria for both methods are objective, these methods provide a rational means for making baseline corrections and obtaining RDGM.

References

Akkar S, Boore DM (2009) On baseline corrections and uncertainty in response spectra for baseline variations commonly encountered in digital accelerograph records. Bull Seismol Soc Am 2009(99):1671–1690

Avallone A, Latorre D, Serpelloni E, Cavaliere A, Herrero A, Cecere G, D'Agostino N, D'Ambrosio C, Devoti R, Giuliani R, Mattone M, Calcaterra S, Gambino P, Abruzzese L, Cardinale V, Castagnozzi A, De Luca G, Falco L, Memmolo A, Migliari F, Minichiello F, Moschillo R, Massucci A, Zarrili L, Selvaggi G (2016) Coseismic displacement waveforms for the 2016 August 24 Mw 6.0 Amatrice earthquake (central Italy) carried out from High-Rate GPS data. Ann Geophys. https://doi.org/10.4401/ag-7275

Boore DM (2001) Effect of baseline corrections on displacements and response spectra for several recordings of the 1999 Chi–Chi, Taiwan earthquake. Bull Seismol Soc Am 2001(91):1199–1211

Boore DM, Bommer JJ (2005) Processing of strong-motion accelerograms: needs, options and consequences, Soil Dynam. Soil Dyn Earthq Eng 25:93–115

Boore DM, Sisi AA, Akkar S (2012) Using pad-stripped acausally filtered strong-motion data. Bull Seismol Soc Am 102:751–760

Chanerley AA, Alexander NA, Halldorsson B (2009) On fling and baseline correction using quadrature mirror filters. In: Topping BHV, Costa Neves LF, Barros RC (eds) Proceedings of the twelfth international conference on civil, structural and environmental engineering computing. Civil-Comp Press, Stirlingshire, Paper 177. Doi:https://doi.org/10.4203/ccp.91.177

Chao WA, Wu YM, Zhao L (2010) An automatic scheme for baseline correction of strong-motion records in coseismic displacement determination. J. Seismol 14:495–504

Cheloni D, Serpelloni E, Devoti R, D'Agostino N, Pietrantonio G, Riguzzi F, Anzidei M, Avallone A, Cavaliere A, Cecere G, D'Ambrosio C, Esposito A, Falco L, Galvani A, Selvaggi G, Sepe V, Calcaterra S, Giuliani R, Mattone M, Gambino P, Abruzzese L, Cardinale V, Castagnozzi A, De Luca G, Massucci A, Memmolo A, Migliari F, Minichiello F, Zarrilli L (2016) GPS observations of coseismic deformation following the 2016, August 24, Mw 6 Amatrice earthquake (central Italy): data, analysis and preliminary fault model. Ann Geophys. https://doi.org/10.4401/ag-7269

Chiaraluce L, Di Stefano R, Tinti E, Scognamiglio L, Michele M, Casarotti E, Cattaneo M, De Gori P, Chiarabba C, Monachesi G et al (2017) The 2016 central Italy seismic sequence: a first look at the mainshocks, aftershocks, and source models. Seismol Res Lett 88(3):757–771. https://doi.org/10.1785/0220160221

ESA (2017) "InSARap Project" http://insarap.org/. Last accessed 2 March 2017

Fiorentino G, Forte A, Pagano E et al (2017) Damage patterns in the town of Amatrice after August 24th 2016 Central Italy earthquakes. Bull Earthq Eng. https://doi.org/10.1007/s10518-017-0254-z

Graizer VM (1979) Determination of the true ground displacement by using strong motion records. Phys Solid Earth 15:875–885

Graizer VM (2010) Strong motion recordings and residual displacements: what are we actually recording in strong motion seismology? Seismol Res Lett 81:635–639

GSI (2016) "The August 2016 Central Italy Earthquake: Crustal deformation detected by ALOS-2 data" http://www.gsi.go.jp/cais/topic160826-index-e.html Last accessed 2 March 2017

INGV (2017). "Earthquake with magnitude of Mw 6.0 on date 24-08-2016." http://cnt.rm.ingv.it/en/event/7073641. Last accessed 31 Oct 2017

INGV Working group "GPS Geodesy (GPS data and data analysis center)" (2016) Preliminary co-seismic displacements for the August 24, 2016 ML6, Amatrice (central Italy) earthquake from the analysis of continuous GPS stations. Zenodo. doi:https://doi.org/10.5281/zenodo.61355

Iwan WD, Chen X (1994) Important near-field ground motion data from the Landers earthquake. In: Proceedings of the tenth European conference on earthquake engineering. Vienna, Austria

Iwan WD, Moser MA, Peng C-Y (1985) Some observations on strong-motion earthquake measurement using a digital accelerograph. Bull Seismol Soc Am 75:1225–1246

Lanzano G, Luzi L, Pacor F, Puglia R, D'Amico M, Felicetta C, Russo E (2016) Preliminary analysis of the accelerometric recordings of the August 24th, 2016 MW 6.0 Amatrice earthquake. Ann Geophys. https://doi.org/10.4401/ag-7201

Luzi L, Puglia R, Russo E, ORFEUS WG5 (2016) Engineering Strong Motion Database, version 1.0. Istituto Nazionale di Geofisica e Vulcanologia, Observatories and Research Facilities for European Seismology. doi:https://doi.org/10.13127/ESM

Luzi L, Pacor F, Puglia R, Lanzano G et al (2017) The Central Italy seismic sequence between August and December 2016: analysis of strong-motion observations. Seismol Res Lett 88(5):1219–1231. https://doi.org/10.1785/0220170037

Makris N, Chang S (2000) Response of damped oscillators to cycloidal pulses. J Eng Mech. https://doi.org/10.1061/(ASCE)0733-9399(2000)126:2(123)

Marinkovic P, Larsen Y (2016) Mapping and analysis of the Central Italy Earthquake (2016) with Sentinel-1 A/B interferometry. Zenodo. https://doi.org/10.5281/zenodo.61133

Michele M, Di Stefano R, Chiaraluce L, Cattaneo M, De Gori P, Monachesi G, Latorre D, Marzorati S, Valoroso L, Ladina C, Chiarabba C, Lauciani V, Fares M (2016) The Amatrice 2016 seismic sequence: a preliminary look at the mainshock and aftershocks distribution. Ann Geophys. https://doi.org/10.4401/ag-7227

Pacor F, Paolucci R, Ameri G, Massa M, Puglia R (2011) Italian strong motion in ITACA: overview and record processing. Bull Earthq Eng. https://doi.org/10.1007/s10518-011-9295-x

Paolucci R, Pacor F, Puglia R, Ameri G, Cauzzi C, Massa M (2011) The Italian CMT dataset from 1977 to the present. In: Akkar S (ed) Earthquake data in engineering seismology, chapter 8, geotechnical, geological and earthquake engineering series, vol 14. Springer, Berlin, pp 99–113

Pischiutta M, Akinci A, Malagnini L, Herrero A (2016) Characteristics of the strong ground motion from the 24th August 2016 Amatrice earthquake. Ann Geophys. https://doi.org/10.4401/ag-7219

ReLUIS-INGV Workgroup (2016) Preliminary study on strong motion data of the 2016 central Italy seismic sequence V6, available at http://www.reluis.it. Last accessed 20 Feb 2017

Rupakhety R, Halldorsson B, Sigbjornsson R (2010) Estimating coseismic deformations from near source strong motion records: methods and case studies. Bull Earthq Eng 8:787–811

Tinti E, Scognamiglio L, Michelini A, Cocco M (2016) Slip heterogeneity and directivity of the ML 6.0, 2016, Amatrice earthquake estimated with rapid finite-fault inversion. Geophys Res Lett 43:10745–10752. https://doi.org/10.1002/2016GL071263

Trifunac MD (1971) Zero baseline correction of strong-motion accelerograms. Bull Seismol Soc Am 61:1201–1211

Wu YM, Wu CF (2007) Approximate recovery of coseismic deformation from Taiwan strong-motion records. J Seismol 11:159–170

Yang S, Mavroeidis GP, Ucak A, Tsopelas P (2017) Effect of ground motion filtering on the dynamic response of a seismically isolated bridge with and without fault crossing considerations. Soil Dyn Earthq Eng 92:183–191, ISSN 0267-7261. Doi:http://dx.doi.org/10.1016/j.soildyn.2016.10.001